High-pressure insulating phase of Mo_4O_{11} with collapsed volume

Z. Y. Liu,[1,2] P. F. Shan,[2,3] K. Y. Chen,[2,3] Madalynn Marshall,[4] S. Zhang,[2,3] T. Yong,[5] H. S. Deng,[6] X. Yin,[6] Y. Ding,[6] H. M. Weng,[2,3] Y. Uwatoko,[7] Przemyslaw Dera,[5] Weiwei Xie,[4] Y. Sui,[1,8,*] and J.-G. Cheng[2,3,†]

[1]*School of Physics, Harbin Institute of Technology, Harbin 150001, China*

[2]*Beijing National Laboratory for Condensed Matter Physics and Institute of Physics, Chinese Academy of Sciences, Beijing 100190, China*

[3]*School of Physical Sciences, University of Chinese Academy of Sciences, Beijing 100190, China*

[4]*Department of Chemistry and Chemical Biology, Rutgers University, Piscataway, New Jersey 08854, USA*

[5]*Hawaii Institute of Geophysics and Planetology, University of Hawaii at Manoa, Honolulu, Hawaii 96822, USA*

[6]*Center for High Pressure Science and Technology Advanced Research (HPSTAR), Beijing 100094, China*

[7]*Institute for Solid State Physics, University of Tokyo, Kashiwa, Chiba 277–8581, Japan*

[8]*Laboratory for Space Environment and Physical Sciences, Harbin Institute of Technology, Harbin 150001, China*

(Received 18 March 2021; revised 12 June 2021; accepted 12 July 2021; published 21 July 2021)

We investigated the effect of pressure on the crystal structure and transport properties of the Magnéli phase η-Mo_4O_{11}, which at ambient pressure undergoes two successive charge-density-wave (CDW) transitions at $T_{\text{CDW-1}} \approx 105$ K and $T_{\text{CDW-2}} \approx 30$ K, respectively. We find that η-Mo_4O_{11} exhibits a structural phase transition from the low-pressure monoclinic $P2_1/a$ phase to a high-pressure $P2_1$ phase at $P_c \approx 3.5$ GPa. Around P_c, the lattice parameters experience a sudden change with a large volume collapse of $\Delta V/V = -8.1\%$, while the room-temperature resistivity exhibits a sudden jump by two orders of magnitude, signaling a pressure-induced metal-to-insulator transition. For $P < P_c$, the high-pressure resistivity measurements revealed opposite pressure dependences of these two CDW transitions, i.e., $T_{\text{CDW-1}}$ is enhanced gradually to ~130 K while $T_{\text{CDW-2}}$ is almost suppressed completely by the application of 2.6 GPa pressure. For $P \geqslant P_c$, the temperature dependence of resistivity changes to an insulating-like behavior, but the activation energy is reduced gradually upon further increasing pressure. We have rationalized the insulating ground state of the high-pressure phase in terms of the structural modifications and charge redistribution based on the refinement of single-crystal x-ray diffraction data at 8.9 GPa.

DOI: 10.1103/PhysRevB.104.024105

I. INTRODUCTION

Pressure and temperature are fundamental parameters that govern the state of matter. The application of high pressure adds an extra dimension on top of varying temperature and/or chemical composition that can expand the phase space of condensed matter, and thus it has been actively utilized in exploring the emergent phenomena of the complex quantum materials. In particular, pressure- and/or temperature-driven phase transitions have been the subject of extensive investigations over the past decades. Here, we report on the observation of pressure-induced structural phase change accompanied by a large volume collapse but an abnormal metal-to-insulator transition in a quasi-two-dimensional (Q2D) metallic oxide, η-Mo_4O_{11}.

η-Mo_4O_{11} belongs to the group of molybdenum suboxides, Mo_nO_{3n-1}, known as the Magnéli phase materials [1], most of which are low-dimensional metals exhibiting interesting physical properties, such as multiple charge-density-wave transitions (CDWs) [2], anisotropic electronic properties [3], and incommensurate-commensurate structural transitions [4]. At ambient conditions, η-Mo_4O_{11} adopts a monoclinic symmetry (space group $P2_1/a$), and the crystal structure consists of infinite slabs of distorted MoO_6 octahedra (ReO_3-type), parallel to the bc plane, connected by MoO_4 tetrahedra along the a^*-axis. The conduction electrons are confined in the octahedral slabs, mainly in the innermost Mo4 sites, which leads to a partially filled conduction band in the bc plane and a Q2D electronic structure with hidden-one-dimensional character [5–7]. Upon cooling down from room temperature, η-Mo_4O_{11} undergoes two successive CDW transitions at $T_{\text{CDW-1}} \approx 105$ K and $T_{\text{CDW-2}} \approx 30$ K, which are associated with the Fermi surface (FS) instabilities with the nesting vectors of $\boldsymbol{q_1} = 0.23\, b^*$ [8] and $\boldsymbol{q_2} = (0.552\, a^*,\ 0.42\, b^*,\ 0.28\, c^*)$ [9], respectively. In the CDW phase below $T_{\text{CDW-2}}$, the Shubnikov–de Haas (SdH) oscillations [10] and bulk quantum Hall effect [11] have been observed and attributed to the presence of very small closed FSs. In addition, anomalous field-induced insulating behavior has been detected above the quantum limit >20 T [12]. Anisotropic negative thermal expansion, occurring along the a^*-axis below $T_{\text{CDW-1}}$, has also been reported [13]. Such peculiar physical properties and behaviors should be associated with the structural and electronic instabilities.

The effects of pressure on the CDW transitions of η-Mo_4O_{11} were studied decades ago via resistivity measurements along the b-axis under hydrostatic pressures up to 1.2 GPa [14]. It was found that these two CDW transitions respond oppositely to the external pressure, i.e., $T_{\text{CDW-1}}$ increases while $T_{\text{CDW-2}}$ decreases progressively with increasing pressure in the investigated pressure range. The distinct

*suiyu@hit.edu.cn
†jgcheng@iphy.ac.cn

responses to pressure underline the difference of dominant mechanisms responsible for these two CDW transitions, and they deserve further investigation. It remains unclear whether further compression would continue shifting the CDW transition at $T_{\text{CDW-1}}$ to higher and higher temperatures, or if it would eventually be suppressed. No structural information was obtained from the previous high-pressure studies to 1.2 GPa, and the structure information as a function of pressure has not been studied above 0.5 GPa so far to our knowledge [15].

Since low-dimensional materials are usually prone to structural instability under high pressure [16,17], we are thus motivated in this work to investigate both the structural and transport properties of η-Mo_4O_{11} in an extended pressure range up to ~14 GPa. In addition to reproducing the previous results, we discovered a hitherto unknown pressure-induced structural phase transition at $P_c \approx 3.5$ GPa, which is accompanied by a large volume collapse of $\Delta V/V = -8.1\%$ and a concomitant metal-to-insulator transition. The observation of a high-pressure insulating phase with a collapsed volume is not a common phenomenon in the complex oxides. Aided by the refinement of single-crystal x-ray diffraction data at 8.9 GPa, we successfully determined the crystal structure of the high-pressure phase with $P2_1$ symmetry and rationalized its insulating ground state in terms of the structural modifications and charge redistribution.

II. EXPERIMENTAL DETAILS

The single crystals of η-Mo_4O_{11} were prepared by the chemical vapor transport method in a two-zone furnace starting from a 1:1 mixture of MoO_2:MoO_3 powders using the $TeCl_4$ as a transport in the temperature region of $T_L = 510$ K and $T_H = 560$ K [18]. Phase purity of the obtained crystals was examined at room temperature by powder x-ray diffraction (XRD), from which the lattice parameters were extracted by the Rietveld refinement method. The temperature dependence of resistivity was measured along the *b*-axis using a standard four-probe configuration.

The *in situ* high-pressure AD-XRD experiments on pulverized crystals were conducted at BL15U1 in Shanghai Synchrotron Radiation Facility (SSRF). The incident x-ray beam energy is 20 keV with a wavelength of $\lambda = 0.6199$ Å. The high pressure was generated by a symmetric diamond anvil cell (DAC) with a pair of Boehler-type 300-μm-culet diamonds. The T301 stainless-steel gasket was compressed to a thickness of 30 μm, and then a 100-μm-diam hole was drilled as the sample chamber. The η-Mo_4O_{11} powder was prepressed to a pellet with a thickness of approximately 10 μm and was then loaded into the sample chamber together with small ruby chips as a pressure marker. Neon was used as the pressure-transmitting medium (PTM) to ensure the hydrostatic pressure environment. MarCCD was used as the detector, and the ruby fluorescence signal was measured to determine the pressure. The CeO_2 standard was employed to calibrate the distance between the sample and the detector and the orientation parameters of the detector. The recorded images were integrated by using the FIT2D program to acquire diffraction intensity versus 2θ data sets. The acquired high-pressure XRD patterns are refined by using the Rietveld method with the General Structure Analysis System (GSAS) program package [19,20].

Single-crystal XRD measurements were carried out on a Bruker Phonon 100 with a home-built DAC high-pressure setup. A $\sim 50 \times 50 \times 20$ μm^3 single crystal of η-Mo_4O_{11} was pressurized with a DAC with a 400-μm culet. Prior to sample loading, the rhenium gasket was preindented to ~40 μm, after which a 250-μm-sized gasket hole was produced using a laser. The PTM is 4:1 methanol:ethanol. Two ruby spheres were subsequently placed next to the sample after it was loaded into the gasket hole, and the pressure inside the DAC was determined through the *R*1 ruby fluorescence line. Data were collected with the DAC axis set to χ at 0° and 90° with an exposure time of 60 s per frame and a 0.25° frame width. The detector distance was maintained at 80 mm. Measurements were taken before and after the expected phase transition at 2.0 and 8.92 GPa. Diffraction data were analyzed with the Bruker SMART software. The single-crystal refinement was done by the SHELXTL package with full-matrix least-squares on the F^2 model. The twin structure has been tested and refined.

Temperature dependences of resistivity measured along the *b*-axis with a standard four-probe configuration were carried out with a palm-type cubic anvil cell (CAC) apparatus under various pressures up to 12.5 GPa. The pressure values in the CAC were estimated from the pressure-loading force calibration curves, which were established by detecting the characteristic phase transitions of Bi (2.55, 2.72, and 7.7 GPa), Sn (9.4 GPa), and Pb (13.4 GPa) at room temperature, or measuring the superconducting transition of Pb at low temperatures. The measured sample was contained in a Teflon capsule filled with glycerol as the PTM. The three-axis compression geometry and the adoption of liquid PTM can ensure a relatively good pressure homogeneity in the whole investigated pressure range. For all the measurements, we always change pressure at room temperature. Details about sample assembly and pressure calibration of CAC can be found elsewhere [21].

III. RESULTS AND DISCUSSIONS

Figure 1(a) displays the synchrotron XRD patterns of Mo_4O_{11} collected at room temperature and under various pressures between 0.5 and 14 GPa. The XRD pattern at 0.5 GPa can be fitted with the ambient-pressure monoclinic structure with a space group $P2_1/a$, Fig. 1(d), which is consistent with the previous study [15]. As seen in Fig. 1(a), the ambient η-phase of Mo_4O_{11} is stable under compression below 2.6 GPa. Upon compression to 4 GPa, two extra peaks emerge at $2\theta \sim 9.8°$ and 10.6°, respectively, indicating the occurrence of pressure-induced structural phase transition, most likely to a lower symmetry. At 5.3 GPa, the XRD pattern is a mixture of two phases, and the diffraction peaks of the high-pressure phase (denoted as η'-phase hereafter) become the main phase. The η'-phase at 7.9 GPa and above can be best indexed with a monoclinic $P2_1$ space group, Fig. 1(b), which was further elaborated by the single-crystal XRD result as shown below. The refinement of the XRD pattern at 5.3 GPa by considering a mixture of η- and η'-phase indicates the ratio of two phases about 1:8, as shown in Fig. 1(c). It should be noted that the

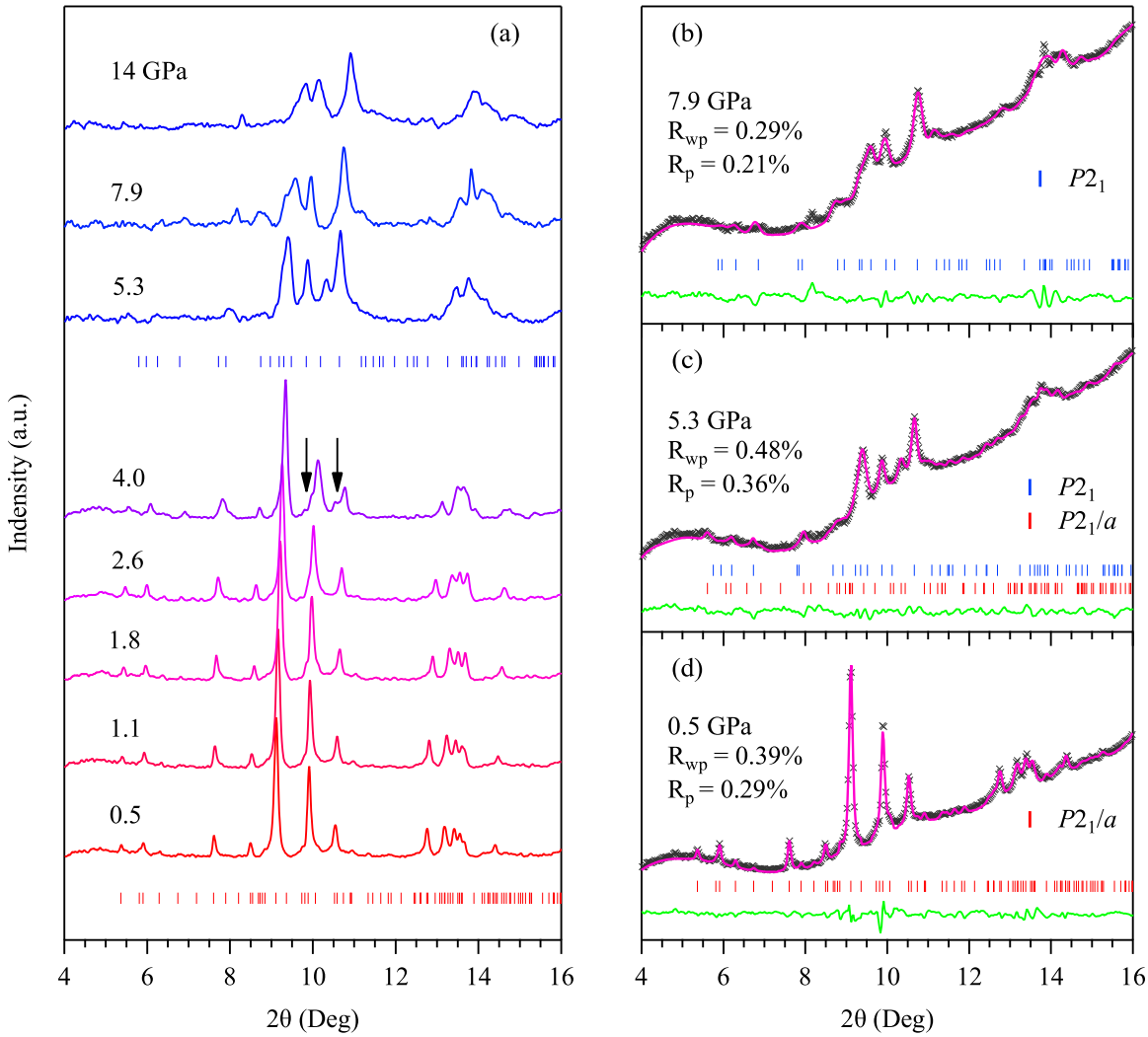

FIG. 1. (a) The background-subtracted diffraction patterns of η-Mo_4O_{11} at high pressures and room temperature. Typical Rietveld refinement results of Mo_4O_{11} under (b) 7.9, (c) 5.3, and (d) 0.5 GPa. The experimental data and fitted XRD profile were shown as black crosses and pink lines, respectively. The marks show the positions of the allowed Bragg reflections for $P2_1/a$ and $P2_1$ phases. The difference between the observed and the fitted XRD patterns was shown with a green line at the bottom of the diffraction peaks.

XRD peaks in the high-pressure η'-phase are broader than those in the low-pressure η-phase, even though we employed the neon PTM. This could be attributed to the presence of microstrain, crystalline defects, and/or nanosized domains across the pressure-induced reconstructive transition around 4 GPa, similar to the situation seen in Cd_3As_2 [22].

Figures 2(a)–2(d) display the pressure dependence of the lattice parameters for the η- and η'-phase. Because the infinite $[Mo_4O_{11}]_n$ layer structure extends along the a-axis, Fig. 2(e) also displays the b/a and c/a axial ratios. Since the unit cell of the η-phase contains 4 formula units (f.u.), while that of the η'-phase contains 2 f.u. due to the reduction of the symmetry and the length of the a-axis by a factor of 2, it is thus more rigorous to describe the change of the volume per formula unit (V/f.u.) across the structural phase transition. With increasing pressure, the lattice parameters a, b, c, β, and V/f.u. contract smoothly within the low-pressure η-phase, and then they experience an abrupt drop on crossing the phase transition to the high-pressure η'-phase at about 4 GPa with a net volume reduction as large as -8.1%. For the η'-phase above 4 GPa, the lattice parameters b, c, and V contract monotonically, whereas the a-axis exhibits an abnormal expansion upon compression. The axial ratios of b/a and c/a are decreasing gradually up to 4 GPa and more drastically at high pressures. The pressure dependence of volume, $V(P)$, for both phases can be fitted with the Birch-Murnaghan equation of state (BM-EOS) [23] as shown by the solid lines in Fig. 2(d). By fixing $B_1 = 4$ in the BM-EOS, we obtained a bulk modulus $B_0 = 39.0(3)$ GPa and V_0/f.u. $= 222.8(2)$ Å^3 for the η-phase, and $B_0 = 56(4)$ GPa and V_0/f.u. $= 199(1)$ Å^3 for the η'-phase, respectively. The high-pressure phase is less compressible than the low-pressure phase.

The pressure-induced structural transition was found to have a profound impact on the electrical transport property. Figure 2(f) shows the pressure dependence of the b-axis resistivity of Mo_4O_{11} measured at room temperature with a CAC. As can be seen clearly, the resistivity jumps abruptly by two orders of magnitude at $P_c \approx 3.5$ GPa, corresponding to the η-to-η' phase transition revealed by the high-pressure XRD measurements. The transition width of $\rho(P)$ around P_c is only

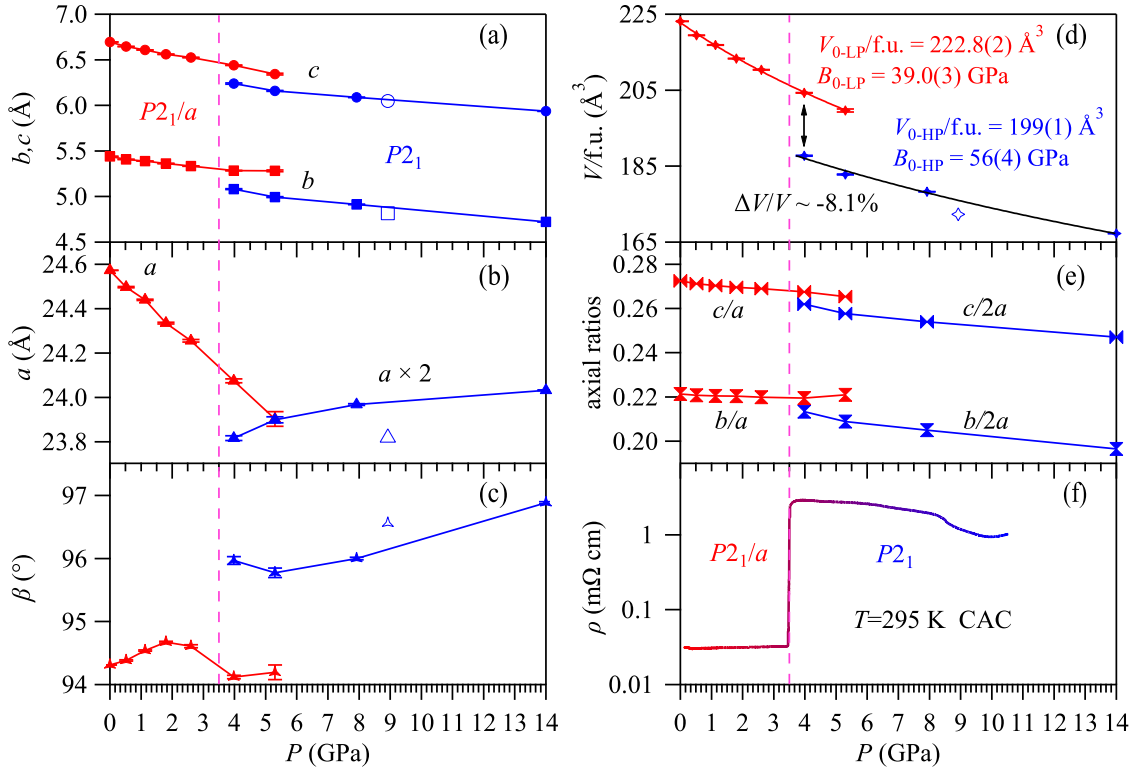

FIG. 2. (a)–(e) Pressure dependences of the lattice parameters, volume per formula unit (V/f.u.), and the axial ratios (c/a and b/a) for the η and η' phases. The open symbols represent the experimental results of the single-crystal sample at 8.92 GPa. The solid lines in (d) represent the fitting results to experimental data by using the Birch-Murnaghan equation of state. (f) The resistivity of Mo_4O_{11} under external pressure from ambient to 11 GPa at 295 K measured with a cubic anvil cell (CAC).

0.1 GPa, reflecting a good pressure homogeneity produced by the CAC. Above P_c, the $\rho(P)$ decreases gradually and exhibits an inflection point at ~9 GPa, above which $\rho(P)$ first decreases at a larger rate and then shows a shallow minimum around 10 GPa followed by an abnormal upturn upon further increasing pressure. Although the enhanced scattering associated with the microstrain, defects, and/or nanosized domains could contribute to some extent to the enhancement of the resistivity across the reconstructive phase transition at P_c, this factor alone cannot explain the sudden jump of resistivity by two orders of magnitude seen in Fig. 2(f). We noted that the resistivity of Cd_3As_2 is only changed by a factor of ~2 across the reconstructive transition [22]. Therefore, we believe that the sudden jump of resistivity at P_c in Mo_4O_{11} should be mainly attributed to an intrinsic change of the electronic structure. The observation of a high-resistance state in the volume-collapsed η'-phase is surprising since the opposite is commonly observed among the complex quantum materials, such as $PbCrO_3$ [24] and $CaMn_2Bi_2$ [25].

To gain more insight into the electrical transport properties of Mo_4O_{11} in both η and η' phases, we have measured the temperature dependence of resistivity with the CAC under various pressures up to 12.5 GPa. Figure 3 shows the $\rho(T)$ curves up to 2.6 GPa within the η-phase. The $\rho(T)$ curve at 0 GPa shows two characteristic anomalies due to the CDW transitions at $T_{CDW\text{-}1} = 104$ K and $T_{CDW\text{-}2} = 31$ K, respectively. With increasing pressure, the anomaly at $T_{CDW\text{-}1}$ moves progressively to higher temperatures, reaching about 130 K at 2.6 GPa, while the anomaly at $T_{CDW\text{-}2}$ is suppressed appreciably both in the magnitude and the transition temperature; the latter transition almost vanishes at 2.6 GPa. These results are in excellent agreement with the previous study [14].

The pressure dependences of $T_{CDW\text{-}1}(P)$ and $T_{CDW\text{-}2}(P)$ determined in the present study together with those from the previous study [14] are displayed in the inset of Fig. 3. As can be seen, $T_{CDW\text{-}1}(P)$ increases with pressure at a rate of $dT_{CDW\text{-}1}/dP = +9.67$ K/GPa, while $T_{CDW\text{-}2}(P)$ decreases at a rate of $dT_{CDW\text{-}2}/dP = -10.92$ K/GPa. No superconductivity was observed down to 1.5 K when the second CDW transition is suppressed completely. It is worth mentioning that the nesting of the first CDW is not perfect, and the remnant FSs almost vanish as a result of the second CDW formation [6]. Therefore, the suppression of the second CDW under pressure is due to the enhancement of the first CDW nesting effect, which results in smaller remnant FSs below $T_{CDW\text{-}1}$ [26,27].

For the η'-phase above P_c, the $\rho(T)$ curves shown in Fig. 4(a) confirm an insulating or semiconducting behavior over the entire temperature range. As can be seen, the $\rho(T)$ at 4.2 GPa (around P_c) increases by two orders of magnitude upon cooling down from room temperature to 1.5 K; the $\rho(T)$ data above 100 K can be described by a thermally activated behavior with an activation energy of $E_g \approx 18$ meV obtained by a linear fitting to $\ln R(T)/R(280)$ versus $1000/T$; see Fig. 4(b). When increasing pressure to 7.9 GPa, the $\rho(T)$ decreases in the whole temperature range, and the E_g is reduced to about 5 meV; see Figs. 4(a) and 4(c). Interestingly, the room-temperature resistivity exhibits an abnormal

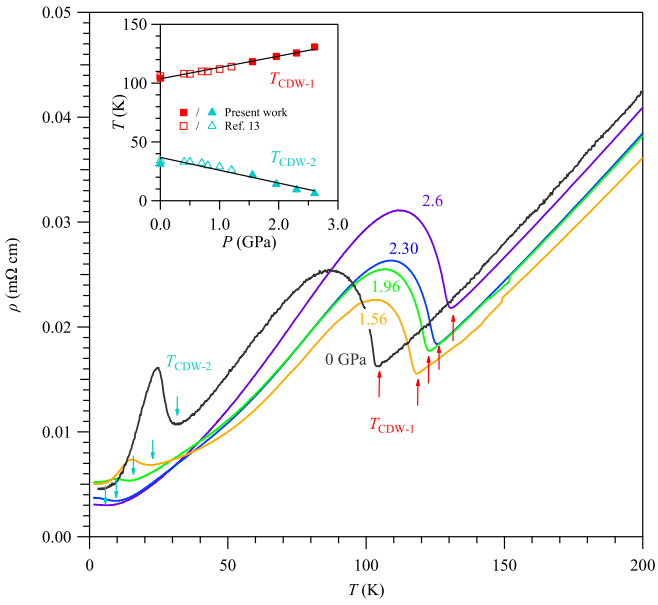

FIG. 3. Temperature dependence of resistivity under various pressures up to 2.6 GPa for η-Mo_4O_{11}. The arrow indicates the CDW transition temperatures. The inset shows the pressure dependence of the CDW transition temperatures $T_{\text{CDW-1}}$ and $T_{\text{CDW-2}}$ determined from the present work and taken from Ref. [14].

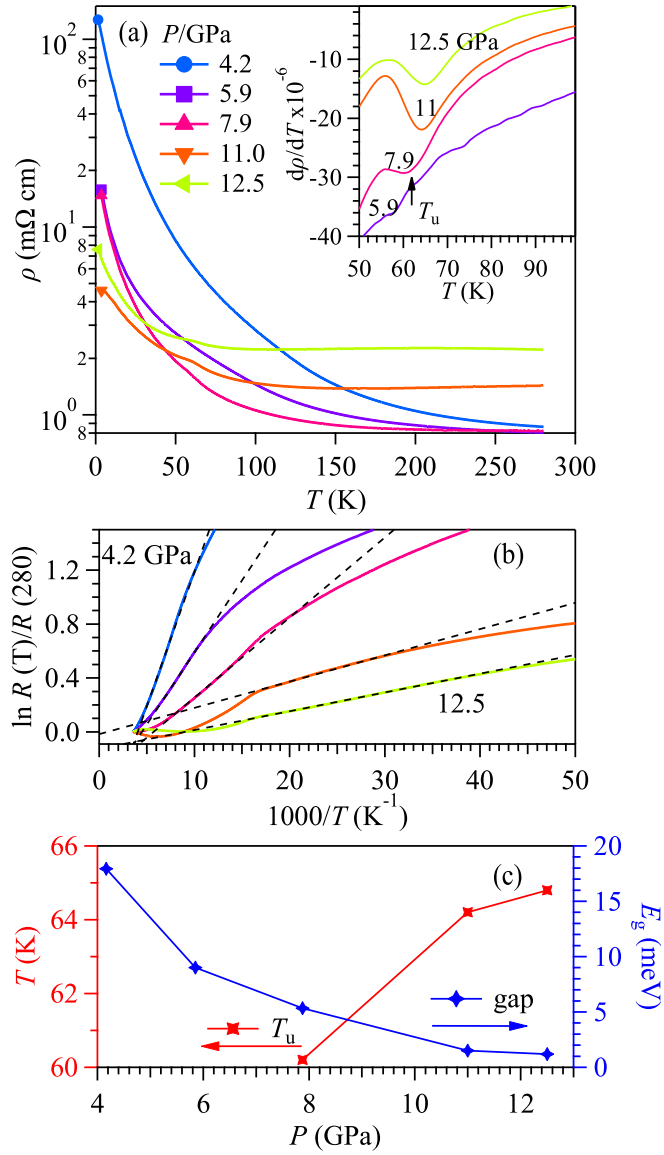

FIG. 4. (a) Temperature dependence of the resistivity $\rho(T)$ under various pressures from 4.2 to 11.8 GPa measured with a palm cubic anvil cell (CAC). The inset shows the $d\rho/dT$ curves and the criterion used for determining the resistivity anomaly temperature T_{u}. (b) A plot of logarithmic form of the normalized resistance vs $1000/T$ for resistivity data. The broken lines in (b) represent the linear fitting curves. (c) Variation with pressure of the activation energy E_{g} and T_{u}.

enhancement upon increasing pressure to 11 GPa and above, and the corresponding $\rho(T)$ curves display a rather weak temperature dependence from room temperature down to ~100 K followed by a relatively quick rise upon further cooling down; see Fig. 4(a). The observed abnormal enhancement of room-temperature resistivity at $P \geqslant 11$ GPa in Fig. 4(a) is consistent with the upturn trend above 10 GPa seen in Fig. 2(f). In addition, there is a clear inflection point at $T_u \approx 65$ K, which can be determined from the minimum of $d\rho/dT$ in the inset of Fig. 4(a). As a result, the $\rho(T)$ curve at $T > T_u$ deviates from the thermally activated behavior, while that at $T < T_u$ can be roughly described by the activated behavior with a reduced $E_{\text{g}} \approx 1$–2 meV, as shown in Figs. 4(b) and 4(c). As a matter of fact, the anomaly at T_{u} is already visible in the $d\rho/dT$ curve of 7.9 GPa. The pressure dependence of T_{u} is shown in Fig. 4(c). The anomalous enhancement of resistivity upon compression and the distinct temperature-dependent behaviors with an anomaly at T_{u} indicate that the η'-phase Mo_4O_{11} might undergo an aberrant electronic transition at ~11 GPa, which deserves further investigations. Considering the electron localization and the presence of unpaired electrons in the η'-phase, the anomaly at T_{u} may correspond to a magnetic transition.

The main finding of the present work is the discovery of a high-pressure η'-phase of Mo_4O_{11} that is characterized by more localized electronic states in a large volume-collapsed structure. This is contrary to the general expectations. For a better understanding of these intriguing properties, it is essential to determine the crystal structure of the η'-phase. To this end, we measured single-crystal XRD at $2.0(< P_c)$ and $8.92(> P_c)$ GPa. The results confirm again that Mo_4O_{11} maintains the monoclinic ($P2_1/a$) structure at 2 GPa, but goes through a phase transition to a monoclinic ($P2_1$) structure at 8.92 GPa, consistent with the synchrotron powder XRD data shown in Fig. 1. The single-crystal XRD data were analyzed with the Bruker SMART software, and the refinement was done by the SHELXTL package with full-matrix least-squares on the F^2 model. The obtained crystallographic data, atomic coordinates, and equivalent isotropic displacement parameters for η'-Mo_4O_{11} under 8.92 GPa are listed in Tables I and II. It is noted that our single-crystal XRD data indicate that the crystal retains a relatively good quality under high pressures. For example, the R_{int} value shown in Table I is only 3% with only 0.19% total reflection rejected; no twinning patterns were observed, and the R values are extremely low even under high

TABLE I. Single-crystal crystallographic data for η'-Mo_4O_{11} at 8.92 GPa.

Formula	Mo_4O_{11}
Temperature (K)	293(2)
F.W. (g/mol)	559.76
Space group; f.u.	$P2_1$ (No. 4); 2
a (Å)	11.909(2)
b (Å)	4.8166(2)
c (Å)	6.0479(4)
β (deg)	96.561(7)
V (Å^3)	344.65(6)
Absorption correction	Numerical
Extinction coefficient	0.008(2)
θ range (deg)	2.675–25.527
h, k, l	$-9 \Leftarrow h \Leftarrow 9$ $-7 \Leftarrow k \Leftarrow 7$ $-7 \Leftarrow l \Leftarrow 7$
No. reflections; R_{int}	4242; 0.0301
No. independent reflections	752
No. parameters	84
R_1; $wR_2[I > 2\delta(I)]$	0.0284; 0.0681
R_1; wR_2 (all)	0.0395; 0.0795
Goodness of fit	1.267
Diffraction peak and hole (e^-/Å^3)	1.048; −0.901

pressure. In addition, all the atomic thermal displacements are consistent under high pressure.

Based on the structural information, we can now make a side-by-side comparison between these two phases and discuss their distinct electronic properties. As shown in Fig. 5(a), the crystal structure of η-phase at low pressures consists of slightly distorted vertex sharing MoO_6 octahedra and MoO_4 tetrahedra. The MoO_6 octahedron is characterized by bond angles ranging from 82(3)° to 98.5(6)° and bond lengths ranging from 1.78(1) to 2.10(1) Å, while the MoO_4 tetrahedron shows bond lengths ranging from 1.74(1) to 1.76(1) Å. There are four independent Mo crystallographic sites, i.e., the tetrahedral Mo1 with a +6 oxidation state and the octahedral Mo2, Mo3, Mo4 with +5.9, +5.6, +5.0 oxidation states, respectively [2,28]. The valence states of the Mo cations were estimated by the Zachariasen formula:

$$D(s) = D(1)(1 - A \ln s),$$

where D is the bond length, $s = Z/N$, Z is the charge, and N is the coordination number of the cation; for the Mo oxides, $D(1) = 1.885$ and $A = 0.166$. The molybdenum oxidation state indicates that the $4d$ electrons should be vanishingly small on the Mo1 sites, and the MoO_4 tetrahedra form the insulating layer, thereby impeding the electronic transport along the a^* direction. In contrast, the Mo4 cations with the +5 oxidation state ($4d^1$) form the zigzag chains along the b-axis, Fig. 5(c), which dominates the electronic transport. In particular, the nearly straight Mo4-O-Mo4 bond angle $\alpha = 171.59°$ along the zigzag chain can facilitate the electronic transport. It is the low-dimensional structural features and the special charge distribution that give rise to a peculiar metallic state with multiple CDW transitions in the low-pressure η-Mo_4O_{11}.

At 8.92 GPa, the structure of the η' phase loses its center of symmetry, and the MoO_4 tetrahedra from the low-pressure structure change to an edge-sharing MoO_5 square pyramid with MoO_6 trigonal prisms as shown in Fig. 5(b). The results are consistent with the tendency that high pressure favors high-density structural arrangements with higher coordination numbers. The structure also consists of distorted vertex sharing MoO_6 trigonal prisms and MoO_5 square pyramids. Bond lengths in the MoO_6 trigonal prisms range from 1.76(3) to 2.11(4) Å, and bond lengths in MoO_5 square pyramids range from 1.73(4) to 2.06(3) Å, respectively. We also estimate the valences of Mo cations at 8.92 GPa by the Zachariasen formula, and the details were listed in Table III. For the η'-phase at 8.92 GPa, the Mo1, Mo2, Mo3, and Mo4 are found to have +5.75, +5.91, +5.87, and +5.4 oxidation states, respectively. In comparison with the η-phase, the $4d$ electrons of η'-Mo_4O_{11} are obviously redistributed and become more uniform under high pressure. Furthermore, the -Mo4-O-Mo4- chains have been distorted from zigzag to armchairlike shape,

TABLE II. Atomic coordinates and equivalent isotropic displacement parameters of η'-Mo_4O_{11} at 8.92 GPa and 293(2) K. U_{eq} is defined as one-third of the trace of the orthogonalized U_{ij} tensor (Å^2).

Atom	Wyckoff	Occupancy	x	y	z	U_{eq}
Mo1	2a	1	0.5595(3)	0.1907(8)	0.1550(2)	0.011(2)
Mo2	2a	1	0.3132(3)	0.1907(7)	0.2254(2)	0.010(2)
Mo3	2a	1	0.1769(3)	0.6898(7)	0.5261(2)	0.009(2)
Mo4	2a	1	0.0658(3)	0.1902(7)	0.8523(2)	0.012(2)
O1	2a	1	0.108(4)	0.014(2)	0.580(3)	Fix.
O2	2a	1	0.206(3)	0.049(2)	0.025(3)	Fix.
O3	2a	1	0.067(3)	0.554(3)	0.339(2)	Fix.
O4	2a	1	0.615(3)	0.501(2)	0.054(3)	Fix.
O5	2a	1	0.672(4)	0.028(2)	0.308(3)	Fix.
O6	2a	1	0.249(4)	0.508(2)	0.267(3)	Fix.
O7	2a	1	0.851(3)	0.016(2)	0.226(3)	Fix.
O8	2a	1	0.009(4)	0.011(2)	0.087(3)	Fix.
O9	2a	1	0.284(3)	0.000(2)	0.460(3)	Fix.
O10	2a	1	0.433(3)	0.485(2)	0.126(3)	Fix.
O11	2a	1	0.470(3)	0.071(2)	0.356(3)	Fix.

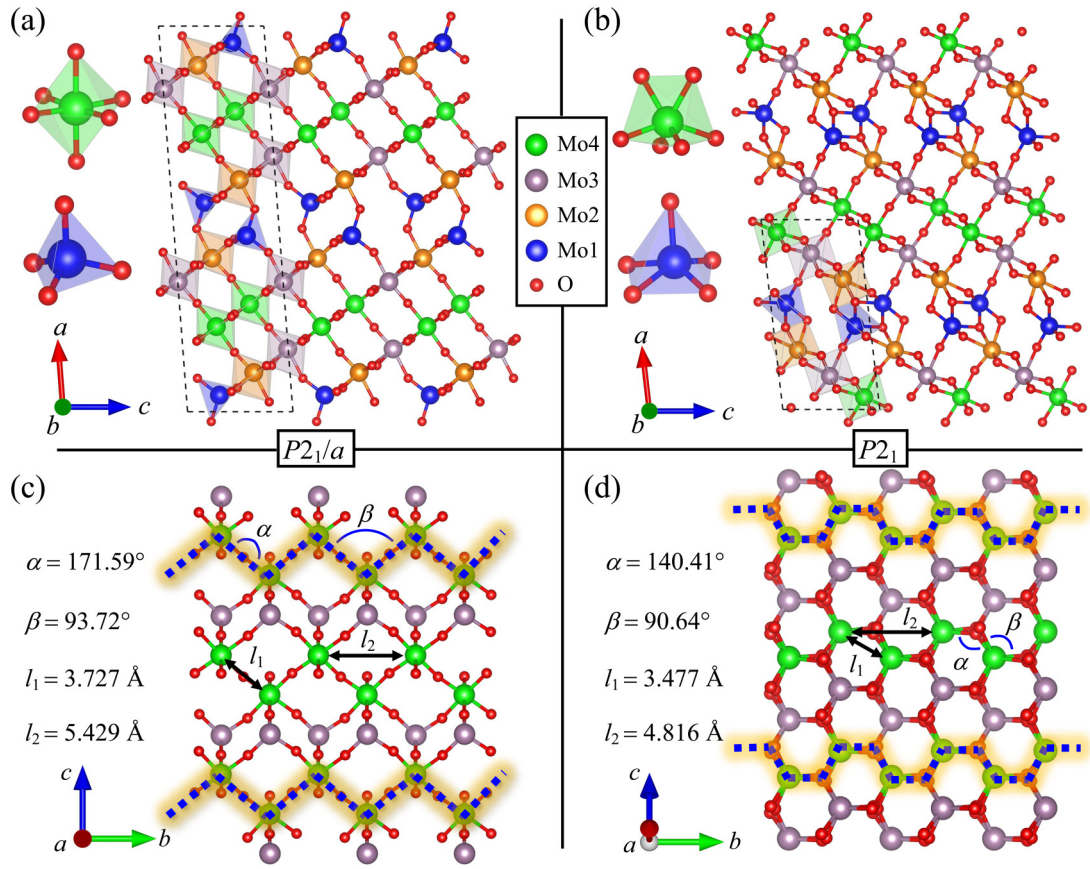

FIG. 5. Schematic crystal structure of (a) η-Mo_4O_{11} with $P2_1/a$ and (b) η'-Mo_4O_{11} with $P2_1$ space group at ambient pressure and 8.92 GPa, respectively. The different Mo cations have been indicated by different colored balls. The red balls are oxygen ions. (c) The top view along the a-axis of the Mo3 and Mo4 sublattice structure of η-Mo_4O_{11} at ambient. The Mo4 and O ions form the infinite -Mo4-O-Mo4- zigzag chains along the b-axis as indicated by the yellow dashed line. (d) The view along the normal to (5 0 −1) of the Mo3 and Mo4 sublattice structural characterization of η'-Mo_4O_{11} at 8.92 GPa with $P2_1$ space group. Armchairlike -Mo4-O-Mo4- chains are marked by the dashed line. α and β are the O-Mo4-O bond angle and Mo4-O-Mo4 bond angle, respectively. l_1 and l_2 are the distances of nearest-neighbor and next-nearest-neighbor Mo4 cations, respectively.

as shown in Fig. 5(d). In this case, the Mo4-O-Mo4 bond angle decreases to 140.41°, which will narrow the bandwidth and may even open a band gap near the Fermi level [29]. From these structural perspectives, we can thus conclude that it is the structural modifications and the charge redistribution that result in the observed semiconducting or insulating behaviors. The further application of high pressure in the η'-phase would broaden the bandwidth and reduce the activation gap as shown in Fig. 4(c). Meanwhile, the structural distortions become more severe under higher pressures such that the localization effect is strengthened, leading to an upturn of resistivity above 10 GPa.

TABLE III. Effective charge per ions estimated by the Zachariasen formula based on bond length for the η'-phase at 8.92 GPa.

	Mo1	Mo2	Mo3	Mo4	$v(i)$
O1			1.28	0.76	2.04
O2		1.36		0.72	2.08
O3			1.50	0.79	2.29
O4	1.46	0.39			1.85
O5	1.64		0.49		2.13
O6		1.60	0.56		2.16
O7			1.41	0.84	2.25
O8(1)				1.16	2.29
O8(2)				1.13	
O9		1.50	0.63		2.13
O10(1)	0.75	0.43			1.76
O10(2)	0.58				
O11	1.32	0.63			1.95
$v(i)$	5.75	5.91	5.87	5.40	

To shed more light on the high-pressure insulating phase, we further calculated the electronic structure of η'-Mo_4O_{11} with the Vienna *Ab initio* Simulation package (VASP) [30,31]. The projector-augmented-wave (PAW) method [32,33], with the Perdew-Burke-Ernzerhof (PBE) exchange-correlation [31] functional, was used. All the calculations are based on the experimental lattice parameters and atomic positions in Tables I and II (the structure from 8.92 GPa single-crystal XRD), and the structure used in the calculation has not been relaxed. We set the plane-wave energy cutoff as 500 eV and a 10 × 8 × 4 k-mesh for high-pressure η'-phase at 8.92 GPa. The band structure is calculated in a nonmagnetic state. For convenience to facilitate the

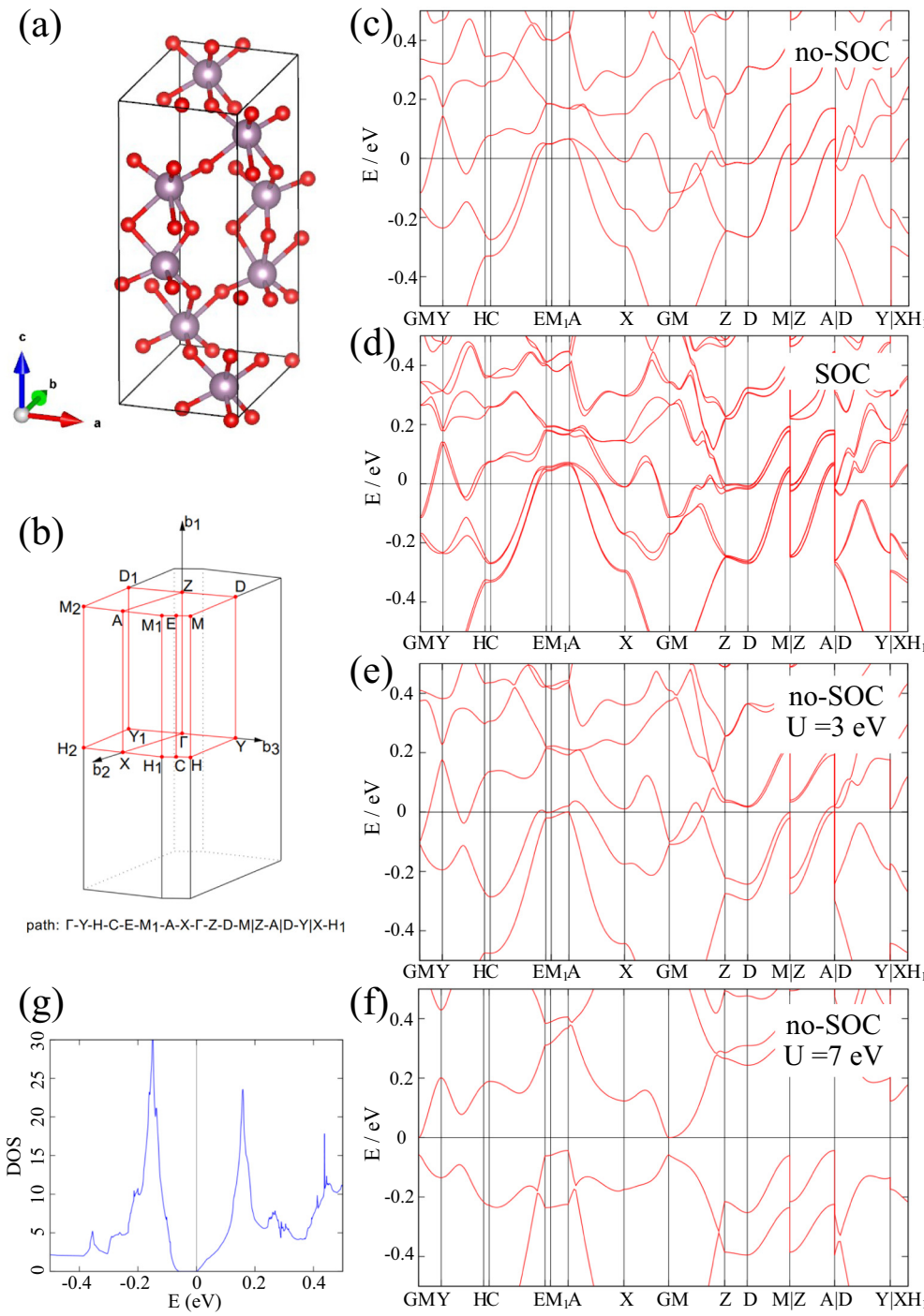

FIG. 6. (a) Crystal structure and (b) Brillouin zone of η'-Mo_4O_{11}. (c,d) The band structure of η'-Mo_4O_{11} without the spin-orbit coupling (SOC) effect and with the SOC effect. (e,f) The band structure of η'-Mo_4O_{11} considering different values of on-site Coulomb interactions energy U. (g) The density of states near the Fermi level with $U = 7$ eV.

calculations, we transform the unit cell and convert the long axis of the crystal structure to the c-axis, as shown in Fig. 6(a), and the Brillouin region is shown in Fig. 6(b). This transformation does not affect the calculation results.

For η'-Mo_4O_{11}, the average valence state of the Mo ion is +5.5, so the band theory requires a metallic state. As shown in Figs. 6(c) and 6(d), regardless of whether the spin-orbit coupling (SOC) effect is considered or not, the energy bands always cross the Fermi level, resulting in a metallic state, which is obviously inconsistent with the experiment result. We also performed additional calculations by considering small variations of the lattice parameters and atomic positions, and we always obtained the metallic ground state. Thus, it is possible that there is a strong electron-electron interaction or other strong correlation effect. In this regard, we consider the on-site Coulomb interaction energy U in the calculation. Without considering the SOC effect, η'-Mo_4O_{11} is still a metal at $U = 3$ eV; but for $U = 7$ eV the band gap is opened and it

presents a semiconducting or insulating state with a vanishing density of states near the Fermi level, as shown in Figs. 6(f) and 6(g). This result strongly suggests that there is a strong electron correlation effect in the pressure-induced η'-phase of Mo_4O_{11}.

IV. CONCLUSION

In summary, we discovered a high-pressure monoclinic insulating phase of Mo_4O_{11} via measurements of synchrotron XRD and electrical resistivity under hydrostatic pressures up to 14 GPa. It is confirmed that the ambient-pressure η-phase with monoclinic $P2_1/a$ symmetry remains stable up to ~3.5 GPa, and the first CDW transition is enhanced monotonically while the second one is suppressed completely by pressure. The high-pressure η'-phase emerges at about 3.5 GPa, where the volume per formula unit shrinks by 8.1% and the resistivity increases by two orders of magnitude at room temperature. In contrast to the η-phase, the η'-phase is characterized by a thermally activated semiconducting behavior with an activation gap decreasing gradually with pressure. The observed small-volume but high-resistance state of η' phase can be rationalized by the structural modifications and more uniform charge redistribution as revealed by the single-crystal XRD refinements. A reentrant electronic localization and possible magnetic order may occur at higher pressure over 10 GPa in the η' phase due to the pressure-induced structural distortions. First-principles calculations also indicate the importance of electron correlations in opening the band gap of the η' phase.

ACKNOWLEDGMENTS

This work is supported by the National Key R&D Program of China (2018YFA0305700), the National Natural Science Foundation of China (12025408, 11874400, 11834016, 11921004, and 11888101), the Beijing Natural Science Foundation (Z190008), the Strategic Priority Research Program and Key Research Program of Frontier Sciences of the Chinese Academy of Sciences (XDB25000000, XDB33000000, and QYZDB-SSW-SLH013), and the CAS Interdisciplinary Innovation Team. The work at Rutgers was supported by the Beckman Young Investigator Award. The single-crystal x-ray diffraction work was conducted using the x-ray Atlas instrument at the University of Hawaii, supported by NSF Grant No. 1541516. Y.S. is supported by the Funds for International Cooperation and Exchange of the National Natural Science Foundation of China (No. 51861135308) and Beijing National Laboratory for Condensed Matter Physics. Y.U. is supported by JSPS KAKENHI Grant No. 19H00648.

[1] L. Kihlborg, Acta Chem. Scand. **13**, 954 (1959).
[2] H. Guyot, C. Escribe-Filippini, G. Fourcaudot, K. Konate, and C. Schlenker, J. Phys. C **16**, L1227 (1983).
[3] M. Sato, K. Nakao, and S. Hoshino, J. Phys. C **17**, L817 (1984).
[4] M. Sato, H. Fujishita, S. Sato, and S. Hoshino, J. Phys. C **19**, 3059 (1986).
[5] G. H. Gweon, S. K. Mo, J. W. Allen, C. R. Ast, H. Höchst, J. L. Sarrao, and Z. Fisk, Phys. Rev. B **72**, 035126 (2005).
[6] N. Hiraoka, T. Buslaps, V. Honkimäki, H. Guyot, and C. Schlenker, Phys. Rev. B **71**, 125417 (2005).
[7] M. A. Valbuena, J. Avila, S. Drouard, H. Guyot, and M. C. Asensio, Appl. Surf. Sci. **254**, 40 (2007).
[8] H. Guyot, C. Schlenker, J. P. Pouget, R. Ayroles, and C. Roucau, J. Phys. C **18**, 4427 (1985).
[9] Y. Nogami, T. Kambe, N. Nagao, and K. Oshima, Synth. Met. **120**, 1049 (2001).
[10] S. Hill, S. Valfells, S. Uji, J. S. Brooks, G. J. Athas, P. S. Sandhu, J. Sarrao, Z. Fisk, J. Goettee, H. Aoki, and T. Terashima, Phys. Rev. B **55**, 2018 (1997).
[11] S. Hill, S. Uji, M. Takashita, C. Terakura, T. Terashima, H. Aoki, J. S. Brooks, Z. Fisk, and J. Sarrao, Phys. Rev. B **58**, 10778 (1998).
[12] M. Sasaki, Y. Hara, M. Inoue, T. Takamasu, N. Miura, G. Machel, and M. von Ortenberg, Phys. Rev. B **55**, 4983 (1997).
[13] H. Negishi, Y. Kuroiwa, H. Akamine *et al.*, Solid State Commun. **125**, 45 (2003).
[14] S. Ohara, M. Koyano, H. Negishi, M. Sasaki, and M. Inoue, Phys. Status Solidi B **164**, 243 (1991).
[15] M. Koyano, S. Ohara, H. Negishi, M. Sasaki, M. Inoue, M. Nomura, and H. Fujiwara, Phys. Status Solidi B **147**, 559 (1988).
[16] Y. Wang, J. Ying, Z. Zhou, J. Sun, T. Wen, Y. Zhou, N. Li, Q. Zhang, F. Han, Y. Xiao, P. Chow, W. Yang, V. V. Struzhkin, Y. Zhao, and H. K. Mao, Nat. Commun. **9**, 1914 (2018).
[17] Z. Yu, L. Wang, Q. Hu, J. Zhao, S. Yan, K. Yang, S. Sinogeikin, G. Gu, and H. K. Mao, Sci. Rep. **5**, 15939 (2015).
[18] H. Negishi, T. Miyahara, and M. Inoue, J. Cryst. Growth **144**, 320 (1994).
[19] B. H. Toby, J. Appl. Cryst. **34**, 210 (2001).
[20] A. C. Larson and R. B. Von Dreele, Los Alamos National Laboratory Report LAUR 86-748 (2004).
[21] J. G. Cheng, K. Matsubayashi, S. Nagasaki, A. Hisada, T. Hirayama, M. Hedo, H. Kagi, and Y. Uwatoko, Rev. Sci. Instrum. **85**, 093907 (2014).
[22] M. Gamża, P. Abrami, L. V. D. Gammond, J. Ayres, I. Osmond, T. Muramatsu, R. Armstrong, H. Perryman, D. Daisenberger, S. Das, and S. Friedemann, Phys. Rev. Mater. **5**, 024209 (2021).
[23] F. Birch, Phys. Rev. **71**, 809 (1947).
[24] J. G. Cheng, K. E. Kweon, S. A. Larregola, Y. Ding, Y. Shirako, L. G. Marshall, Z. Y. Li, X. Li, A. M. dos Santos, M. R. Suchomel, K. Matsubayashi, Y. Uwatoko, G. S. Hwang, J. B. Goodenough, and J. S. Zhou, Proc. Natl. Acad. Sci. (USA) **112**, 1670 (2015).
[25] X. Gui, G. J. Finkelstein, K. Chen, T. Yong, P. Dera, J. Cheng, and W. Xie, Inorg. Chem. **58**, 8933 (2019).
[26] M. Inoue, S. Ohara, S. Horisaka, M. Koyano, and H. Negishi, Phys. Status Solidi B **148**, 659 (1988).

[27] J. Beille, U. Beierlein, J. Dumas, C. Schlenker, and D. Groult, J. Phys.-Condens. Matter **13**, 1517 (2001).
[28] W. H. Zachariasen, J. Less-Common Met. **62**, 1 (1978).
[29] J. B. Torrance, P. Lacorre, A. I. Nazzal, E. J. Ansaldo, and C. Niedermayer, Phys. Rev. B **45**, 8209 (1992).
[30] G. Kresse and J. Furthmüller, Phys. Rev. B **54**, 11169 (1996).
[31] J. P. Perdew, K. Burke, and M. Ernzerhof, Phys. Rev. Lett. **77**, 3865 (1996).
[32] P. E. Blöchl, Phys. Rev. B **50**, 17953 (1994).
[33] G. Kresse and D. Joubert, Phys. Rev. B **59**, 1758 (1999).